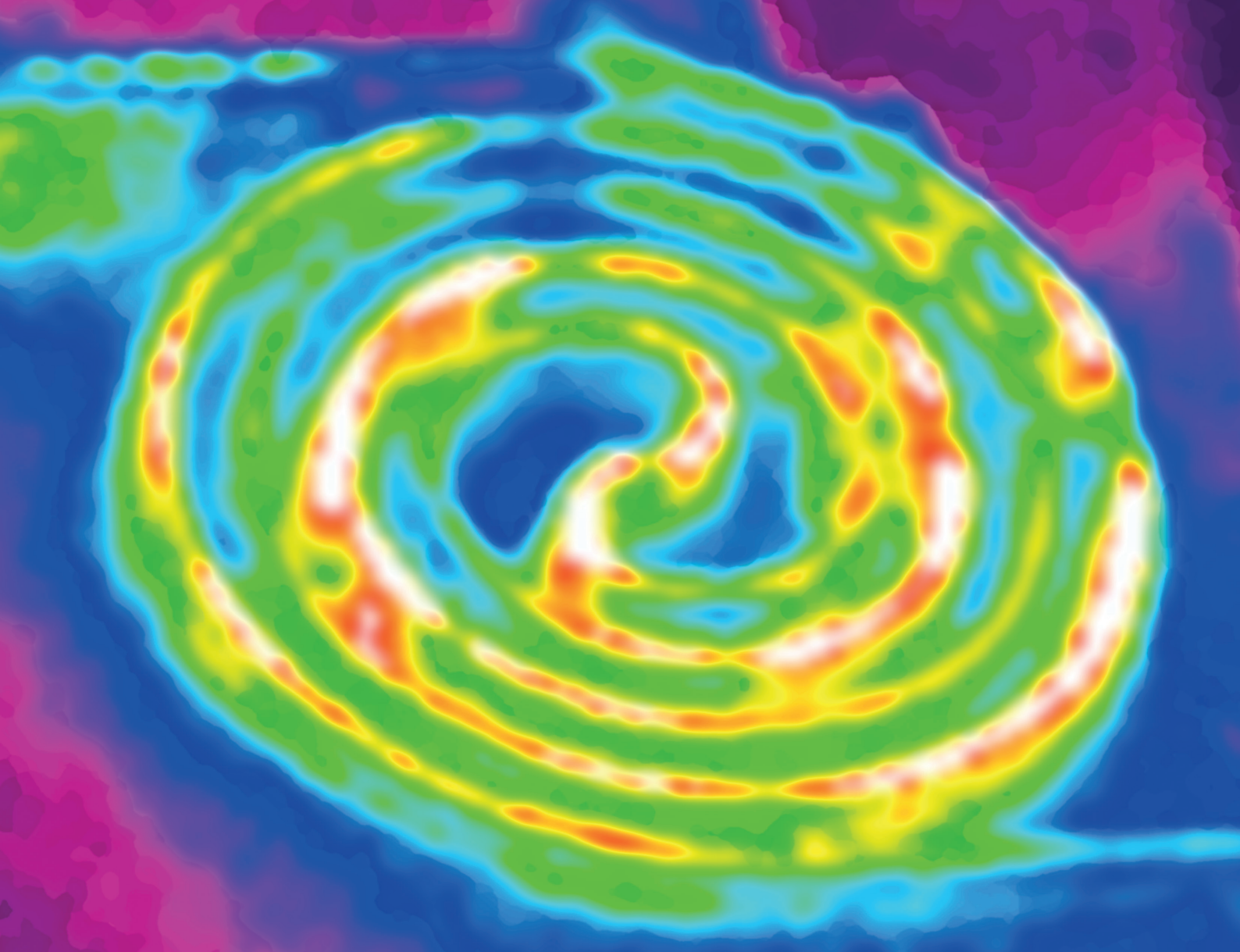


ADVANCED MATERIALS

In article number 1801584, Weidong Zhou, John A. Rogers, and co-workers report flexible, transient optical waveguides constructed from monocrystalline silicon, for precise delivery of light to targeted biological tissues, at dimensions that can approach those of a single cell, with the ability to undergo controlled bioresorption into benign products after a well-defined operational time, thereby serving as building blocks for silicon-based bioresorbable photonic systems, with potential broad applicability in diagnosis and therapy.



Flexible Transient Optical Waveguides and Surface-Wave Biosensors Constructed from Monocrystalline Silicon

Wubin Bai, Hongjun Yang, Yinji Ma, Hao Chen, Jiho Shin, Yonghao Liu, Quansan Yang, Irawati Kandela, Zhonghe Liu, Seung-Kyun Kang, Chen Wei, Chad R. Haney, Anlil Brikha, Xiaochen Ge, Xue Feng, Paul V. Braun, Yonggang Huang, Weidong Zhou,* and John A. Rogers*

Optical technologies offer important capabilities in both biological research and clinical care. Recent interest is in implantable devices that provide intimate optical coupling to biological tissues for a finite time period and then undergo full bioresorption into benign products, thereby serving as temporary implants for diagnosis and/or therapy. The results presented here establish a silicon-based, bioresorbable photonic platform that relies on thin filaments of monocrystalline silicon encapsulated by polymers as flexible, transient optical waveguides for accurate light delivery and sensing at targeted sites in biological systems. Comprehensive studies of the mechanical and optical properties associated with bending and unfurling the waveguides from wafer-scale sources of materials establish general guidelines in fabrication and design. Monitoring biochemical species such as glucose and tracking physiological parameters such as oxygen saturation using near-infrared spectroscopic methods demonstrate modes of utility in biomedicine. These concepts provide versatile capabilities in biomedical diagnosis, therapy, deep-tissue imaging, and surgery, and suggest a broad range of opportunities for silicon photonics in bioresorbable technologies.

The interaction of light with biological materials provides a powerful, broadly useful basis for clinical diagnosis and therapy.^[1–3] The highly scattering and absorbing nature of most biological tissues limit, however, the ability to transmit light of certain desired wavelengths to targeted regions at depth, to control its directionality or polarization properties, and to form focused images.^[4] Implantable optical waveguides can address these challenges, but the permanent nature of the materials conventionally used in such systems is problematic for applications that require only temporary diagnostic or therapeutic function, due to the need for secondary surgical extraction. Recent work demonstrates possibilities in bioresorbable waveguides constructed from natural or synthetic macromolecular

Dr. W. Bai, Prof. J. A. Rogers
Department of Materials Science and Engineering
Northwestern University
Evanston, IL 60208, USA
E-mail: jrogers@northwestern.edu

Dr. W. Bai, Q. Yang, Dr. J. Shin, Prof. Y. Huang, Prof. J. A. Rogers
Center for Bio-Integrated Electronics
Northwestern University
Evanston, IL 60208, USA

Dr. H. Yang, Dr. Y. Liu, Z. Liu, Dr. X. Ge, Prof. W. Zhou
Department of Electrical Engineering
University of Texas at Arlington
Arlington, TX 76019-0072, USA
E-mail: wzhou@uta.edu

Prof. Y. Ma, Prof. X. Feng
Department of Engineering Mechanics
Center for Mechanics and Materials
Tsinghua University
Beijing 100084, China

Prof. H. Chen, Prof. P. V. Braun
Department of Materials Science and Engineering
Frederick Seitz Materials Research Laboratory
Beckman Institute for Advanced Science and Technology
University of Illinois Urbana-Champaign
Urbana, IL 61801, USA

Dr. J. Shin
Department of Chemical and Biomolecular Engineering
University of Illinois Urbana-Champaign
Urbana, IL 61801, USA

Q. Yang, C. Wei, Prof. Y. Huang
Department of Mechanical Engineering
Northwestern University
Evanston, IL 60208, USA

Dr. I. Kandela
Center for Developmental Therapeutics
Northwestern University
Evanston, IL 60208, USA

Prof. S.-K. Kang
Department of Bio and Brain Engineering
Korea Advanced Institute of Science and Technology
Daejeon 34141, Republic of Korea

C. Wei, Prof. Y. Huang
Department of Civil and Environmental Engineering
Northwestern University
Evanston, IL 60208, USA

Dr. C. R. Haney, A. Brikha
Chemistry Life Processes Institute
Northwestern University
Evanston, IL 60208, USA

 The ORCID identification number(s) for the author(s) of this article can be found under <https://doi.org/10.1002/adma.201801584>.

DOI: 10.1002/adma.201801584

materials such as silk fibroin, poly(lactide-co-glycolide) (PLGA), and poly(L-lactic acid) (PLA).^[5,6] Key drawbacks include susceptibility to swelling as a result of water uptake and limited contrast in index of refraction, the latter of which can lead to poor optical mode confinement and propagation losses in tissues and biofluids.^[4] Here, we introduce the use of lithographically defined, thin filaments of monocrystalline silicon (m-Si) as low loss, dimensionally stable and bioresorbable optical waveguides that avoid many of these limitations and, through lithographic modifications, allow for localized spectroscopic evaluation of biochemistry.

Silicon photonic devices in the form of mechanically rigid chips are well established in lightwave systems for telecommunications, in optical data interconnects for high-speed electronics, and in sensors for chemical/biological detection.^[7] Recent research establishes the ability to create and assemble nanoscale forms of m-Si, typically nanomembranes (NMs), nanoribbons (NRs), or nanowires (NWs), for hybrid, flexible, and stretchable electronic devices, thereby enabling applications that cannot be addressed by conventional wafer platforms.^[8–10] Related work highlights similar possibilities in photonics,^[11–13] where flexible photonic crystal microcavities on plastic substrates represent one interesting example.^[14,15] As an optical material, m-Si is attractive compared to polycrystalline, amorphous, or nanoporous Si due to its low propagation losses and its ability to be engineered into geometries that create well-defined evanescent waves for applications in optical sensing.^[16,17]

The results presented here combine concepts from this collective body of prior work with recent approaches that use nanoscale forms (typically nanomembranes, NMs) of m-Si as bioresorbable, active materials in physically transient classes of electronic devices.^[18,19] Here, hydrolysis of Si yields orthosilicic acid (Si(OH)₄),^[19,20] a compound naturally found in the human body.^[21] Hybrid integration of Si NMs with other organic and inorganic bioresorbable materials yields high-performance electronic systems with proven biocompatibility and clinically relevant modes of operation,^[19,22] as an emerging type of biomedical implant that disappears, without risk to the patient, after a relevant operational time period. Polymers such as PLGA represent attractive choices for substrate and encapsulation materials,^[5,23] where the time for degradation can be tailored from a few minutes to over a year by altering their molecular weight and the ratio of their monomer constituents.^[24] The products of ester hydrolysis are lactide and glycolide monomers, both of which possess excellent tissue compatibility and can be metabolized by the body.^[24]

The technology outlined in the following relies on methods for forming long, thin filamentary structures of m-Si from Si NMs, patterned to unwind from dense, planar coiled layouts. The high refractive index of silicon enables tight optical mode

confinement at sub-micron scales, thereby enabling precise delivery of light to targeted tissues, at dimensions that can approach those of a single cell.^[25] The addition of PLGA as a cladding layer yields extended, mechanically flexible, bioresorbable waveguides with low propagation losses even when embedded in biological tissues. From an optical standpoint, the cladding restricts access of the evanescent field to the surroundings; from a mechanical standpoint it locates the core material at the neutral mechanical plane of the structure. Locally exposing the m-Si cores of these waveguides allows controlled interactions between the evanescent fields and the surrounding environment, to provide capabilities for optically sensing the local chemistry.^[26,27] Engineered waveguide curvature at the core yields extended evanescent fields, increased interactions and, therefore, improved sensitivity of the measurement.^[28] Specifically, the absorption of near-infrared (NIR) light (750–2500 nm) by biological materials produces spectral signatures associated with overtones and combinations of molecular vibrations due to O–H, C–H, and N–H groups, thereby yielding critical information on the chemical composition of nearby biomolecular species.^[29] These spectroscopic data provide the basis for precise, label-free, continuous, and reliable diagnostics of diseased tissues,^[2,30] of particular value during and after surgery or treatment. Systematic studies reveal all the key optical, mechanical, biosensing, and processing aspects of these platforms.

Figure 1 summarizes the key steps for forming such types of flexible m-Si transient optical waveguides through a series of schematic illustrations and corresponding tilted-angle, colorized scanning electron microscopy (SEM) images, with more details shown in the Supporting Information. The procedure begins with photolithography and reactive ion etching (RIE) to define m-Si waveguide structures from the top device layer of a silicon-on-insulator (SOI; Figure 1a) wafer. Immersion in concentrated hydrogen fluoride (HF) solution for 2 min fully removes the exposed buried oxide (BOX) and partially undercuts this layer near the edges of the m-Si waveguides (Figure 1b). Spin-coating a layer of positive tone photoresist (PR), flood exposing to ultraviolet light, and inserting into a developer solution removes the PR everywhere except beneath the m-Si at the perimeter, partially undercut regions (Figure 1c). This residual PR serves to physically tether the m-Si structures to the underlying substrate but still allows HF to pass, thereby enabling full undercut etching of the remaining BOX layer (Figure 1d). Transfer printing with stamps of poly(dimethylsiloxane) (PDMS) enables delivery of the m-Si filaments onto substrates of PLGA (thickness: $\approx 10 \mu\text{m}$) prepared by slowly drying a solution of this material on a hydrophobic surface (e.g., Si substrate with a self-assembled monolayer formed using trimethoxymethylsilane). Laminating another layer of PLGA (thickness: $\approx 10 \mu\text{m}$) on top and annealing under a vapor of ethyl acetate effectively lowers the glass transition temperature of the PLGA to allow bonding between the top and bottom layers. Laser milling defines the lateral boundaries of strips of PLGA with the m-Si core at the center. This process not only forms an optical cladding, but also it positions the Si near the neutral mechanical plane to minimize the strain induced by bending.

Bending mechanics is important not only for use of these waveguides in biological studies but also for their efficient

Prof. J. A. Rogers
Department of Biomedical Engineering
Department of Neurological Surgery
Department of Electrical Engineering and Computer Science
Department of Mechanical Engineering, and Department of Chemistry
Simpson Querrey Institute for BioNanotechnology
Northwestern University
Evanston, IL 60208, USA

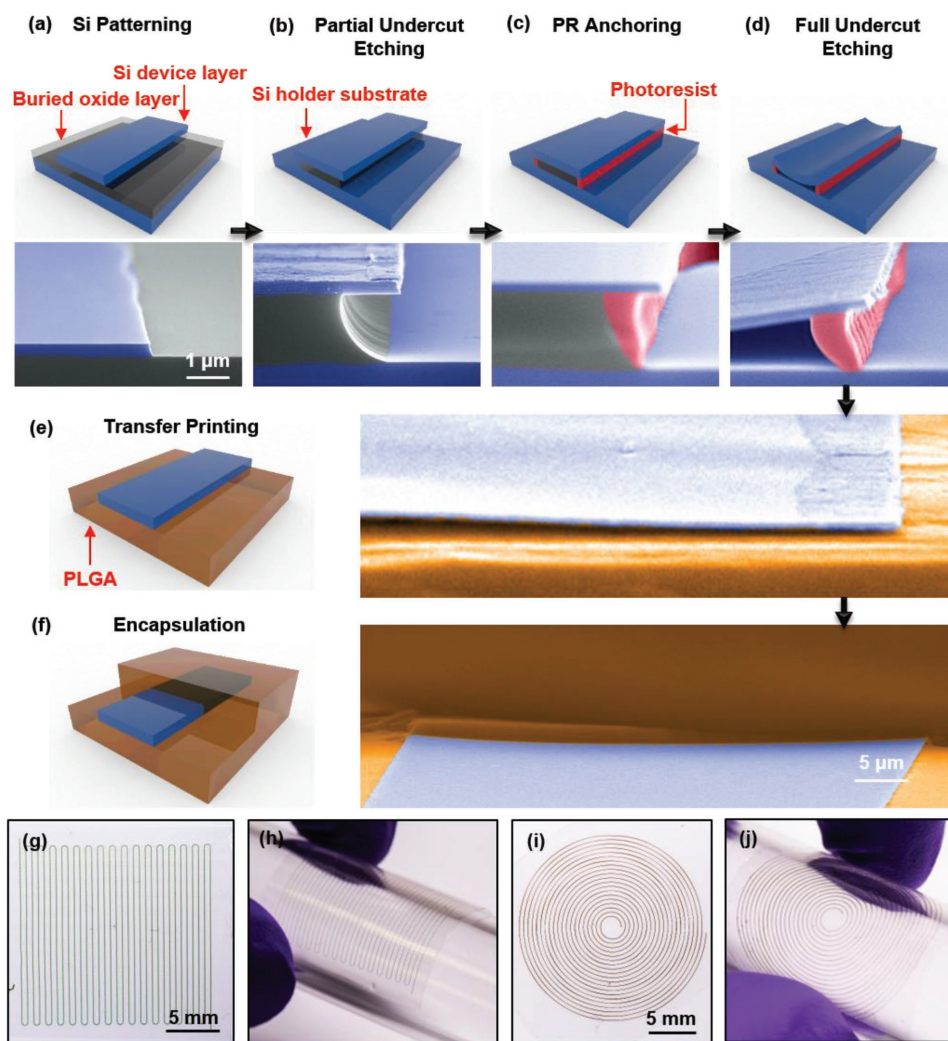


Figure 1. Schematic illustrations and colorized SEM images of key steps for fabricating flexible silicon transient optical waveguides. a) Photolithography and reactive ion etching define Si filamentary waveguides from the Si device layer (200 nm thick) of a silicon-on-insulator substrate. b) Controlled etching using hydrofluoric acid consumes the exposed buried oxide (BOX) layer and partially undercuts the BOX layer underneath the edges of the waveguides. c) Spin-coating a positive photoresist (PR), flood exposing, and inserting the substrate into a developer leave a thin strip of PR underneath the edges of the waveguides. d) Further etching removes the remaining BOX layer, thereby leaving the waveguides supported only by the PR structures. e) A PDMS stamp allows retrieval of the waveguides and exposure of their back sides such that immersion in acetone eliminates any residual PR. Physical transfer integrates the waveguides onto a layer of PLGA. f) Lamination of another layer of PLGA on top and exposure to solvent vapors of ethyl acetate seals the PLGA layers to thereby encapsulate the waveguide. g,h) Optical images of a zigzag waveguide with 32 turning corners. The thickness, width, and contour length of the Si core are 200 nm, 50 μm , and 72.6 cm, respectively. i,j) Optical images of a spiral waveguide with base radius 1 mm, top radius 1 cm, and 20 turns. SEM images of (a)–(e) share the same scale bar. The colorized regions in the SEM images correspond to silicon (blue), buried oxide (gray), photoresist (red), and PLGA (brown).

fabrication. Specifically, by configuring the m-Si filaments into zig-zag or spiral shapes (Figure 1g–j), it is possible to efficiently utilize the SOI and, via a process of unfurling and stretching, form waveguides that are much longer than the characteristic dimensions of the wafer. Based on the source materials (SOI, PLGA, etc.) and the fabrication processes, a rough estimation suggests that the cost of waveguides formed in this manner can be as low as ≈ 6 USD foot^{-1} , compatible with envisioned applications in clinical medicine. With similar zigzag or spiral designs, increasing the density can further increase the unfurled length for a given patterned area, limited mainly by practical considerations associated with the widths

of the laser-milled strips of PLGA. Figure 1g,i shows examples of zigzag and spiral shapes with high packing densities, where the total lengths of the Si cores are 54.4 and 72.6 cm, respectively.

Figure 2 summarizes theoretical and experimental analyses of the mechanical properties of various waveguides and their processes for unfurling, with a focus on three different configurations (labeled I, II, and III). Figure 2a–c highlights finite element analysis results (FEA, ABAQUS commercial software)^[31] and experimental demonstrations of the unfurling of waveguides with m-Si cores (elastic modulus 130 GPa and Poisson's ratio 0.27) that have thicknesses and widths of 1500 nm and

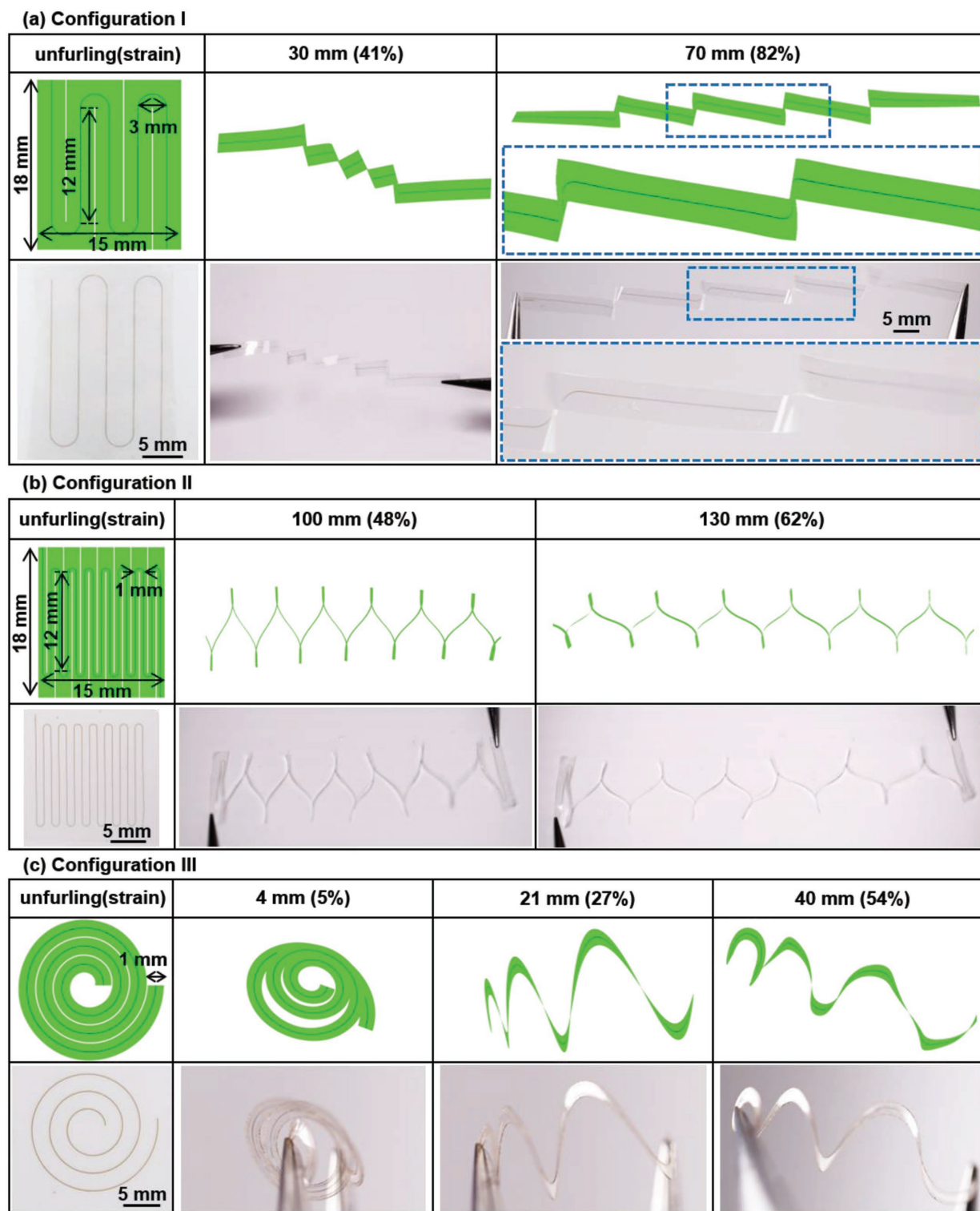


Figure 2. Geometrical design and mechanical analysis of flexible silicon transient optical waveguides. a–c) Finite element analysis (FEA) results and optical images of the process of unfurling structures with zigzag and spiral shapes (Configuration I–III). Left column: Schematic illustration with key dimensions in the undeformed state. The Si core (width and thickness 50 μm and 1500 nm, respectively) lies at neutral plane of the PLGA cladding (thickness 20 μm). Unfurling strain: the ratio of the total end-to-end distance of the unfurled structure to the overall length of the Si core. a) Configuration I, zigzag waveguide with four turning corners. The thickness, width, and length of the Si core are 1500 nm, 50 μm , and 20.9 cm, respectively. b) Configuration II, zigzag waveguide with 14 turning corners. Thickness, width, and length of the Si core are 1500 nm, 50 μm , and 54.4 cm, respectively. c) Configuration III, spiral waveguide, with base radius 1.5 mm, top radius 8.5 mm, and 3 turns. Thickness, width, and length of the Si core are 1500 nm, 50 μm , and 7.3 cm, respectively.

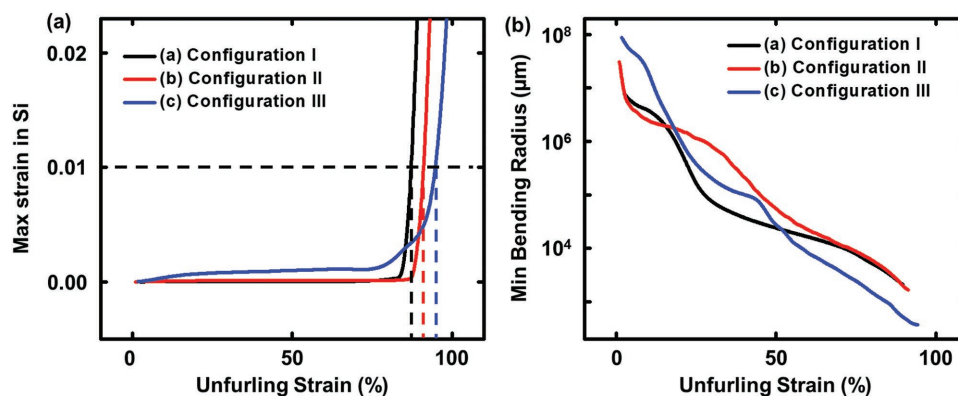


Figure 3. Mechanical simulations of flexible silicon transient optical waveguides. a) Plot of maximum strain in the Si as a function of unfurling strain for each configuration. A maximum strain of 1% corresponds to the fracture point of the Si. b) Plot of the minimum (out-of-plane) bending radius as a function of unfurling strain for each configuration.

50 μm , respectively, embedded at the neutral plane of 20 μm thick PLGA strips (elastic modulus 2 GPa and Poisson's ratio 0.36)^[32] with widths of 3 mm for Configuration I and 1 mm for Configuration II and III. Configuration I, which corresponds to a zigzag geometry in the undeformed state, yields a distribution of strain induced by unfurling as shown in Figure 3a. Here, strains in the m-Si appear mainly at each turning point for unfurling strains up to $\approx 70\%$ (as defined by the ratio of the total end-to-end distance of the unfurled structure, to the overall length of the m-Si cores). Above this value, further unfurling begins to generate global strains, eventually leading to fracture of the m-Si at $\approx 87\%$ (the point at which the maximum strain in the Si core reaches 1%, the fracture strain of Si^[9]). The PLGA remains in a regime of elastic deformation throughout this process. In this geometry, the m-Si core is largely straightened, except for regions near the turning points (Figure S1a, Supporting Information). Experimentally, this unfurling process demonstrates the high level of flexibility that can be achieved without fracturing the m-Si, consistent with FEA simulation (Figure 2a). Figure 2a shows the unfurled shape for Configuration I, where the total end-to-end distance (unfurled length) is ≈ 70 mm (unfurling strain of $\approx 82\%$; contour length of the m-Si core ≈ 85 mm). A zigzag design with enhanced packing density (Configuration II) appears in Figure 2b. Here, the total contour length of the m-Si is 208 mm, and the other parameters (thickness, width of m-Si core, area of SOI wafer usage, and thickness of PLGA cladding) are the same as those for Configuration I. As in FEA simulation (Figure S1a,b, Supporting Information), Configuration II can unfurl to an end-to-end distance of 190 mm, corresponding to a maximum unfurling strain (91%) that is slightly higher than that for Configuration I (87%).

Spiral designs (Configuration III, Figure 2c) yield improved uniformity in strain distribution along the m-Si, thereby offering increased extension in unfurling. In particular, for the same physical parameters (PLGA thickness and width, and cross-sectional dimensions of the Si) FEA simulations indicate that spiral designs (Configuration III) can support unfurling strains of up to 96%. As with the zigzag shapes, the maximum unfurling strain can be increased by increasing the packing density of the m-Si cores while keeping the other parameters (thickness, width of m-Si core, area of SOI wafer usage, and

thickness of PLGA cladding) the same. As shown in Figure S1d (Supporting Information), a spiral shape with enhanced packing density (the total contour length of Si is 24.0 cm) can achieve 99% unfurling strain. For the spiral shapes, unfurling generates strains that initiate around the outer rings and then gradually propagate to the inner rings of the spiral geometry (Figure S1c,d, Supporting Information).

All three configurations (I, II, III) show slow increases in strain in the m-Si upon unfurling, with a maximum strain in the m-Si of $\approx 0.001\%$ for Configuration I and II and 0.01% for Configuration III at 85% unfurling strain. Figure 3a shows the corresponding maximum strain in m-Si as a function of unfurling strain, based on FEA simulation. An abrupt increase in strain in the m-Si appears at high unfurling strain (typically $>85\%$), where unfurling strains of 87, 91, and 96% reach the fracture threshold for m-Si, for Configuration I, II, and III, respectively.

Unfurling in all cases induces bending. Due to the large differences between the thicknesses and the widths of these waveguides, the flexural rigidity in the in-plane direction (parallel to the top or bottom surface of the Si core, as illustrated in Figure S2, Supporting Information) is 10^5 times larger than that in the out-of-plane direction. As a result, unfurling mostly involves bending in the latter direction. Figure 3b shows that the minimum (out-of-plane) bending radius in the m-Si decreases as the unfurling strain increases. At the maximum unfurling strain, the minimum bending radius can reach 2070, 1666, and 370 μm , for Configuration I, II, and III, respectively (Figure 3b). Simulations indicate that the optical loss associated with unfurling (corresponding to out-of-plane bending at bending radius 370 μm and above) is negligible (around 0.05 dB cm^{-1}), compared with the loss associated with absorption in the PLGA cladding and scattering from imperfections in the m-Si filamentary structures (around 0.7 dB cm^{-1} in total, details are in the Supporting Information). Specifically, unfurling the waveguides (Configuration I–III) has little effect on their optical properties, partly due to the high degree of mode confinement provided by the high index of refraction of the m-Si cores.

Figure 4 summarizes the optical performance characteristics of the waveguides. Butt coupling to a silica optical fiber allows

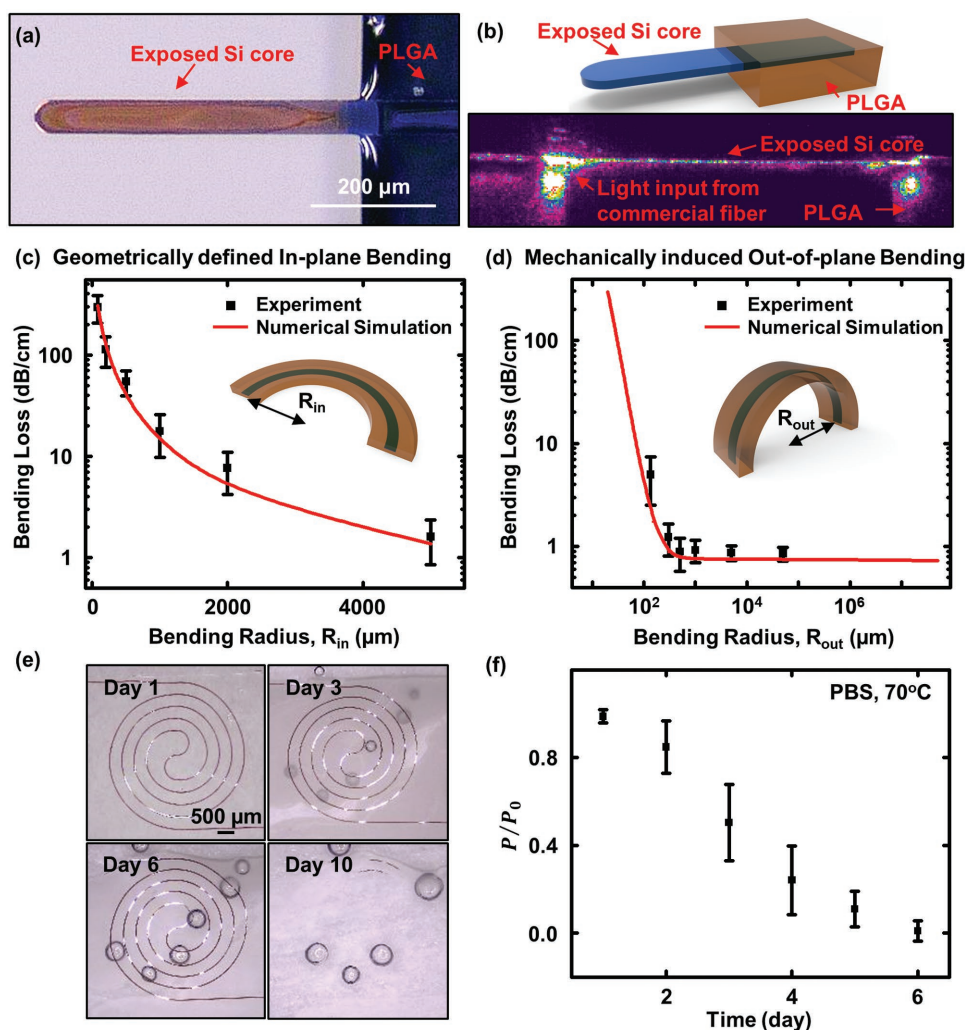


Figure 4. Measurements of propagation losses through flexible silicon transient optical waveguides and their dissolution. a) Optical microscopy image of the short, exposed segment of the Si core at the tip end of the waveguide, formed by stripping the PLGA cladding; b) Upper: schematic illustration of the exposed tip of the Si core. Bottom: image of propagation of near-infrared light (wavelength: 1550 nm) from the end of a commercial fiber to the tip of the Si core. The image was recorded using an infrared camera (Ophir Optics LLC). c) Experimental and simulation results of the bending loss as a function of geometrically defined in-plane bending radius (R_{in} , defined in the inset schematic illustration). The simulation assumes a roughness $\sigma = 30$ nm on the edges of the Si cores. d) Experimental and simulation results of the bending loss as a function of mechanically induced (out-of-plane) bending radius (R_{out} , defined in the inset schematic illustration). Simulation assumes Si sidewall roughness $\sigma = 30$ nm. e) Dissolution of a spiral waveguide structure during immersion in phosphate-buffered saline (PBS) at 70 °C. Optical images captured at day 1, 3, 6, and 10 indicate a uniform process of hydrolysis of the Si filaments. Imperfect lamination of the spiral waveguide on the surface leaves small air bubbles trapped underneath the PLGA, which gradually become more obvious as the dissolution of PLGA proceeds. All images share the same scale bar. f) Optical measurements of the waveguide under similar conditions: P : measured output intensity. P_0 : the highest measured output intensity at day 1.

for introduction and extraction of light (Figure S3, Supporting Information). Removing the PLGA cladding leaves a short, exposed segment of the m-Si core (Figure 4a,b, and Figure S3c, Supporting Information) to facilitate coupling. Here, a transparent adhesive (Norland Optical Adhesive 81) bonds the aligned fiber to the m-Si, thereby minimizing relative motions and lowering coupling losses caused by the mismatch between the refractive index of the fiber (1.44) and the m-Si (3.48) (Figure S4, Supporting Information) (Figure S3d, Supporting Information, illustrates the improvements in coupling that follow from the use of the adhesive). The exposed m-Si tip can also be utilized as an optical sensor or stimulator (Figure S5, Supporting Information).

Figure S6 (Supporting Information) demonstrates propagation of light (wavelength 633 nm) along the waveguide, launched at the tip end. Three main factors contribute to optical loss:^[33] (i) scattering, which arises mainly from the surfaces of the m-Si, as determined by surface roughness, typically at the scale of tens of nanometers for standard photolithography, or localized imperfections associated with the fabrication process; (ii) radiation, which follows from the electromagnetic profiles of the propagating modes, and can be significant for curved or sharply bent waveguides; and (iii) absorption, from interband, band edge, and free-carrier effects in the m-Si core and PLGA cladding. The cut-back method^[34] yields values for the propagation losses at a wavelength of 1550 nm, as a function of the

width of the m-Si core (thickness 1500 nm). The results indicate losses of $\approx 0.7 \text{ dB cm}^{-1}$, comparable to losses for conventional m-Si waveguides formed in the usual manner on SOI platforms.^[35,36] Experiments and simulations indicate that the losses for waveguides reported here with core thicknesses of 1500 nm do not depend strongly on the width of the core for values between 20 and 100 μm , consistent with a negligible role of random roughness on the sidewalls of the m-Si core (Figure S7, Supporting Information). Systematic studies of the effects of surface roughness (Figures S7 and S9, Supporting Information), and of curvature and bending, provide additional details.

Bending and unfurling can lead to changes in curvature and associated losses. Examining the effects of in-plane curvature involves studies of a group of waveguides (1500 nm thick and 50 μm wide Si cores) with two, lithographically defined, 90° bends located near the midpoint of the overall length, with radii between 80 and 5000 μm (Figure S9f, Supporting Information). Figure 4c shows experimental and simulation results for the associated losses. This form of loss becomes significant only for radii below $\approx 2000 \mu\text{m}$ (Figure 4c, and Figure S10a, Supporting Information). As shown in Figure S10c,d (Supporting Information), in-plane bending leads to concentration of propagating modes near the outer convex boundary of the core, resulting in radiation losses. As a result, the turning corners for the zigzag waveguides (Configuration I and II, the in-plane bending radii at turning corners are 1500 and 500 μm , respectively) contribute most significantly to the total loss. For spiral waveguides (Configuration III), the bending loss gradually increases from the outer ring (top radius 8500 μm) to the inner ring (base radius 1500 μm). For m-Si cores with thicknesses of 1500 nm and widths of 50 μm , maintaining the in-plane curvature radii to values larger than $\approx 2000 \mu\text{m}$ ensures low bending-induced losses. Reducing the width (over a range, in this case, 1–100 μm for 1500 nm thick Si cores) of the core can increase the in-plane confinement of the propagating modes, thereby further reducing the bending loss (Figure S11a, Supporting Information).

Figure 4d and Figure S10b–d (Supporting Information) summarize experimental and simulation results for out-of-plane bending. Here, the measurements focus on straight, flexible waveguides (1500 nm thick, 50 μm wide Si cores, Figure S9g, Supporting Information) with out-of-plane bending radii achieved by wrapping around glass rods with radii between 130 and 50 000 μm . Experiments show negligible loss in cases with out-of-plane bending radii 300 μm and above, and radically increased loss in case with bending radii 130 μm , consistent with simulations. Numerical studies suggest significant loss only for radii smaller than 10 and 130 μm for waveguides with 50 μm wide m-Si cores and thicknesses of 200 and 1500 nm, respectively (Figure S10b, Supporting Information). These critical bending radii are much smaller than those of previously reported bioresorbable waveguides,^[5] simply due to the large index of refraction of the m-Si core (compared to the cladding). For bending radii below these critical values, the propagating mode distributions shift to the outer convex boundary of the core, thereby leading to increases in propagation loss (Figure S10c,d, Supporting Information). Unfurling the zig-zag waveguides

(Configuration I and II, Figure 2) induces bending of the m-Si cores at the turning points, while the spiral shape generates bending globally. Across the entire range of unfurling strains (from 0 to $\approx 85\%$) for Configurations I, II, and III (Figure 2), the minimum out-of-plane bending radii are ≈ 2000 , 1600, and 370 μm , respectively. These radii are much larger than the critical values (110 μm) determined by simulation, consistent with the low losses observed experimentally in the test structures. Compared with the loss induced by in-plane curvature (Figure S10a, Supporting Information), that from out-of-plane bending shows little dependence on the width of the m-Si core (over a range, in this case, 5–100 μm for 1500 nm thick m-Si cores) for a wide range of bending radii (Figure S11b,c, Supporting Information), due to the strong confinement of propagating modes at out-of-plane direction.

In addition to their mechanics during unfurling and deployment, a key defining feature of these systems is their bioresorbability. Immersion in phosphate buffered saline (PBS, pH 7.4) illustrates the processes that lead to complete dissolution to biocompatible end products. Figure 4e shows an accelerated lifetime test of a spiral waveguide sensor (Si core with thickness 1500 nm, width 50 μm , supported by a 10 μm thick PLGA film; details on the construction and sensing performance described in the next paragraph) in PBS at 70 °C. By day 3, the PLGA exhibits a dramatic decrease in transparency, consistent with swelling, water uptake, and initial stages of hydrolysis. The Si filament dissolves by a comparatively uniform process of hydrolysis, as shown in the optical images in Figure 4e. Full dissolution occurs within 10 d, consistent with previously reported dissolution rates for Si (from the Si device layer on SOI wafer, p-type (boron), orientation (100), SOITEC) of $\approx 5 \text{ nm d}^{-1}$ and $\approx 140 \text{ nm d}^{-1}$ in PBS at 37 and 67 °C, respectively.^[20] From the standpoint of waveguiding properties, losses for the spiral waveguide in PBS at 70 °C increase sharply due to dissolution of the Si filament and scattering in the PLGA (Figure 4f). By day 6, the loss prevents effective waveguiding (Figure 4f).

As in the structure described above (Figure 4f), an optical biosensor can be formed from the waveguides simply by removing the PLGA cladding in a local region to expose the m-Si core to the surroundings (Figure 5a,b). The evanescent field, concentrated near the outer surface of the m-Si, allows interactions with surrounding materials in this exposed region, thereby modulating the light propagation in a way that depends on the optical characteristics of these materials (Figure S12a–c, Supporting Information). Absorption and/or scattering associated with interactions of the evanescent field depends on both the real part (n) and imaginary part (κ , extinction coefficient) of the complex refractive index of materials in contact with the m-Si. The latter imposes well-defined features in the spectral characteristics of light transmitted through the transient biosensor, thereby yielding important information on the chemistry and concentration of these materials.^[37,38] The sensitivity depends on the strength of the evanescent field at the interface, as measured by the spatial confinement factor (Figure S12d, Supporting Information). As shown in Figure S12 (Supporting Information), for a straight m-Si waveguide, reducing the thickness or the width decreases the spatial confinement factor. For a curved waveguide, shifts (e.g., from

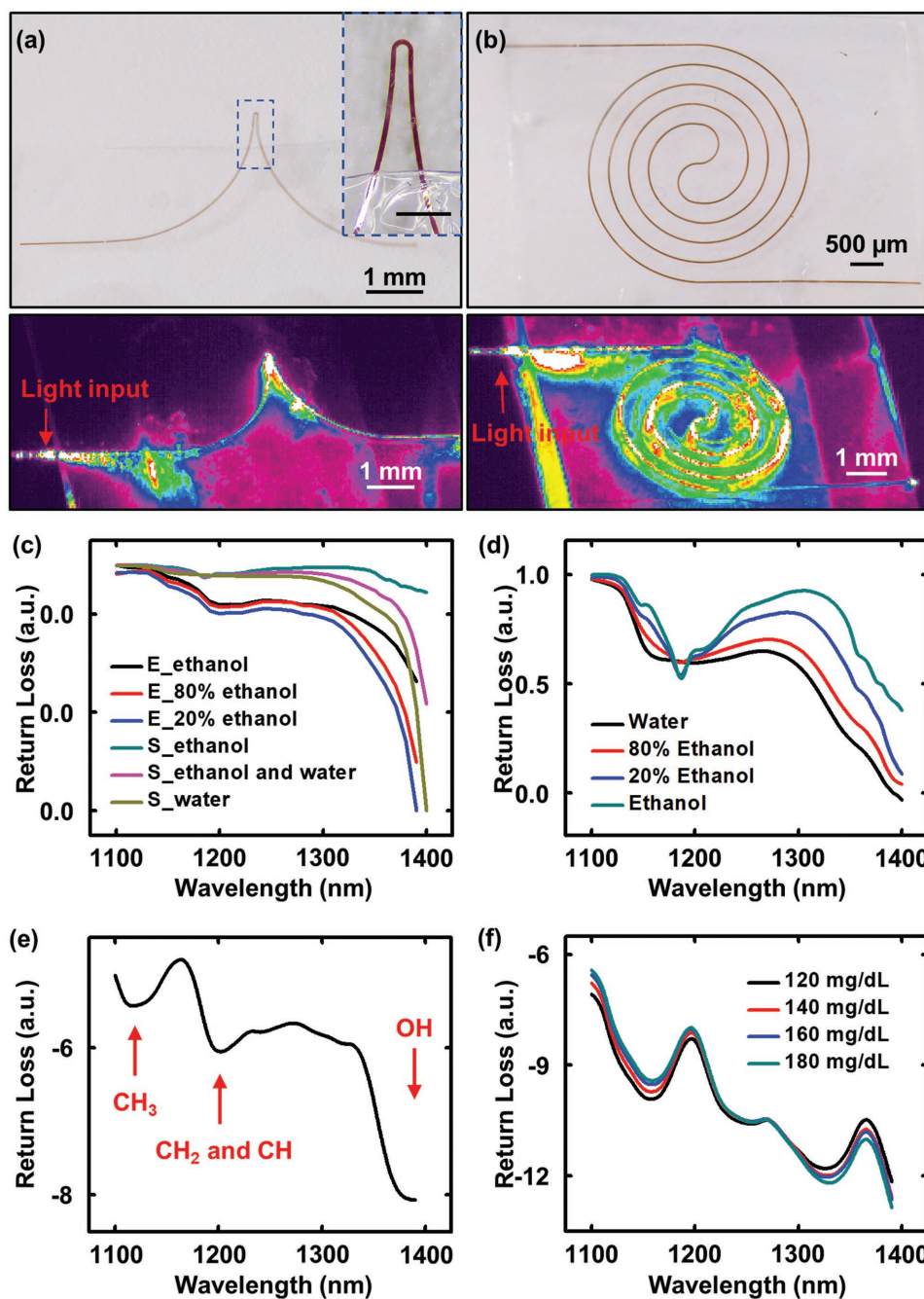


Figure 5. Transient Si waveguide-based biosensor. a) Optical sensor that uses a PLGA-clad Si waveguide with an exposed (top, bottom, and side surfaces) region that has a U shape (thickness 1500 nm, width 50 μm) where the evanescent field interacts with the surrounding environment. Inset: enlarged view of this sensing region. Scale bar: 300 μm . b) Similar device but with a sensing region that adopts a spiral shape, with the Si core exposed on the top and side surfaces, with a 10 μm thick film of PLGA on its base. (a) and (b) Upper: Optical microscopy image of the sensing region. Lower: propagation profile of near-infrared light (1550 nm) through this region. c) Experimental and simulation results of the transmission spectrum of a U-shaped transient biosensor immersed in a mixture of water and ethanol, as measured in terms of the return loss. E_ethanol, E_80% ethanol, and E_20% ethanol are experimental measurements; S_ethanol, S_ethanol, and water, and S_water are simulation results. d) Transmission spectrum of a mixture of water and ethanol measured with a UV-vis-NIR spectrometer (Perkin Elmer LAMBDA 1050). e) Transmission spectrum measured in terms of the return loss of a spiral-shaped transient biosensor immersed in photodefinable epoxy (SU8). f) Transmission spectrum measured in terms of return loss of a spiral-shaped transient biosensor immersed in mouse blood with different concentrations of glucose.

the center of the core to the boundary of it) and/or conversions (e.g., from lower-order modes to higher-order modes) of propagating modes can occur due to distortions of the optical fields

in the regions of bending (Figure S10c,d, Supporting Information), thereby resulting in enhanced evanescent fields and further decreases in the spatial confinement factor.^[33]

Figure 5 shows spectra measured by transmission through transient biosensors with exposed Si regions that adopt U-shapes (exposed above and below) and spiral shapes (exposed top) (Figure 5a,b). The spiral device (Figure 5b) exposes a larger area (around 4.5 mm²) of m-Si than the U-shape (around 0.4 mm²) (Figure 5a), thus offering a larger sensing area. The U-shape, by contrast, is capable of localized sensing responses. The lower part of Figure 5a highlights the concentrated leakage of light at the tip of the U-shape biosensor, while the spiral-shape biosensor shows leakage uniformly distributed around its spiral geometry (lower part of Figure 5b). Figure 5c shows good agreement between the experimental and simulation results for the case of a U-shaped device in sensing of ethanol, water, and their mixtures. Some intrinsic wavelength-dependent losses in the waveguide affect the output spectrum in a way that is not captured by the simulations.^[37] Figure 5d shows the transmission spectrum measured using a conventional NIR spectrometer (Perkin Elmer LAMBDA 1050). The characteristic features are consistent with those in the spectrum measured by the transient biosensor. Discrepancies likely arise mainly from wavelength-dependent penetration depths of the evanescent field and variations in the real part of the refractive index near the absorption band of the surrounding materials.^[37]

The spectrum of a photodefinable epoxy (SU8, Microchem) measured using a spiral device shows absorption bands at 1120, 1210, and 1390 nm corresponding to the second overtone regions of CH₃, CH₂, CH, and OH groups associated with the epoxy (Figure 5e), consistent with the known spectra of this material.^[39] In one envisioned example, the transient biosensor can insert into deep tissue to provide continuous monitoring of parameters such as glucose concentration for a certain time, followed by dissolution. The medical relevance is that poor management of glucose levels in extracellular fluids can cause metabolic disorders. If not diagnosed and treated, this condition can lead to cardiovascular disease, damage to blood vessels, stroke, blindness, chronic kidney failure, nervous system failure, ulceration, and early death.^[40] NIR spectroscopy has some utility in blood glucose monitoring due to the presence of characteristic absorption features associated with glucose. Directed targeting of this sensing modality at designated tissue locations, especially for locations at depth,^[41] can be difficult or impossible with skin-mounted devices. Figure 5f demonstrates the ability to sense glucose with a transient Si waveguide-based biosensor over a range of concentrations in mouse blood from 120 to 180 mg dL⁻¹, which is relevant to normal range for humans (70–180 mg dL⁻¹). Increasing the glucose concentration results in characteristic spectral changes, especially in terms of increased absorption at 1400 nm due to the vibrational resonance of the OH group. For all sensing measurements, aligning fibers to the input and output ends of the transient biosensor uses an assembly of optomechanical hardware (Ficontec, Inc., Figure S3a, Supporting Information) followed by epoxy bonding. Calibration curves corresponding to return loss at wavelengths of 1160 and 1330 nm exhibit linearity across a relevant range of glucose concentrations (from 120 to 180 mg dL⁻¹, Figure S13, Supporting Information). This simple measurement allows glucose concentration to be determined with an uncertainty of ≈15 mg dL⁻¹, thereby providing good sensitivity for medically relevant changes. For practical

use, interfering effects associated with absorption by other biological species must be considered.^[42] Figure S13 (Supporting Information) summarizes each step of data processing for the transmission spectra measured by the device, with details described in the Experimental Section.

Deploying these transient biosensors in live animal models highlights capabilities for continuous optical sensing of blood oxygenation via transmission spectroscopy in the near-infrared range (1000–1200 nm). Figure 6a shows a transient biosensor that consists of a U-shaped Si waveguide supported by a film of PLGA with the top surface of the Si exposed. A pair of optical fibers constructed with bioresorbable polymers (PLGA; labeled Fiber 1 and Fiber 2 in Figure 6a–c) bond (Ficontec) in an aligned fashion to the input and output ports of the Si waveguide to inject light at wavelengths of 1050 nm (Fiber 1) and 1200 nm (Fiber 2) and to collect signals from the other fiber (Figure 6b). In vitro tests of hemoglobin in PBS saline at various oxygenation levels demonstrate the required measurement sensitivity (Figure 6d), even at concentrations that are ten times lower than those in human blood. Calibration curves corresponding to absorption at 1050 and 1200 nm show a linear response from 5 to 100% blood oxygen saturation (Figure 6e). Inserting the transient biosensor into the subcutaneous region near the thoracic spine and connecting the fibers to external light sources and optical power meters configures the system for measurements (Figure 6b,c). Figure 6f shows results from tests that involve changing the concentration of oxygen in the surrounding environment to trigger corresponding changes in the oxygen saturation of the blood (SO₂) measured by the transient biosensor, consistent with the measurement of a commercial oximeter positioned at the paw of the mice. The measurement uncertainty is ≈4% SO₂, mostly arising from motion artifacts, tissue heterogeneities, and venous pulsations.

The flexibility of the device enables conformal contact with subcutaneous tissue, thus minimizing mechanically induced irritation and enhancing the measurement interface. Figure 6f and Figure S16d (Supporting Information) show a series of computed X-ray tomography (CT) images at various times after implantation from day 1 to day 15. The results clearly show a gradual disappearance of the device by processes of bioresorption. A notable point concerning these platforms is their ability to support spectroscopic evaluations, as a route to improved sensitivity and capabilities for measuring additional biochemical species.

The silicon transient optical waveguide and biosensor platforms introduced here provide unique capabilities of relevance to a broad range of applications in biomedicine and biological research by virtue of their mechanical flexibility and bioresorbable nature. The use of monocrystalline silicon, derived from wafer-scale sources of high quality material, represents a key advantage compared to alternative approaches. The unfurling process, optimized to account for bending strains and bending-induced optical losses, represents an enabling feature of the fabrication process. Biosensing of important biochemical species, including glucose and oxygenated/deoxygenated hemoglobin by NIR spectroscopic methods, through in vitro and in vivo studies of physiologically relevant ranges, highlights the potential utility of these platforms in biomedicine. Long-term use requires a controlled delay in the initiation of

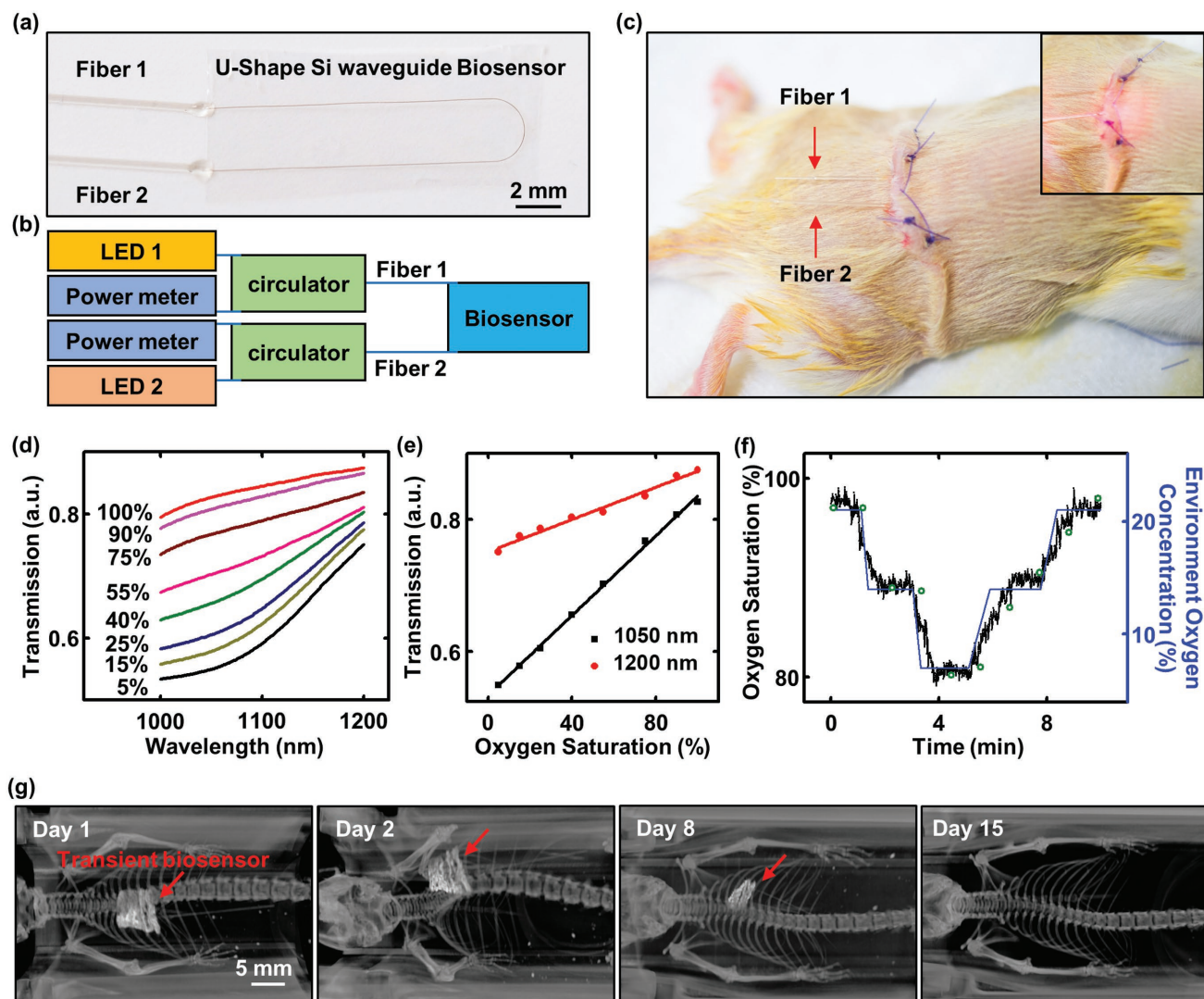


Figure 6. Monitoring of blood oxygen saturation in a live animal model using a transient Si waveguide-based biosensor. a) Image of a transient biosensor. Two bioresorbable fibers connect to a U-shaped Si waveguide bonded to a film of PLGA with its top surface exposed. b) Schematic illustration of the operating principles: Each of the two bioresorbable fibers (labeled Fiber 1 and Fiber 2), probing externally from the transient biosensor, connects via a fiber circulator to a light source (1050 nm wavelength for Fiber 1, and 1200 nm wavelength for Fiber 2) and a power meter for delivering and detecting light, respectively. c) Image of a transient biosensor implanted into the subcutaneous region near the thoracic spine of a mouse. Inset: image of red light (wavelength: 660 nm) passing into the biosensor. d) In vitro measurements of oxygenation of hemoglobin in phosphate-buffered saline (PBS) by near-infrared absorption measurements using a transient biosensor. Hemoglobin concentration: 1.5 g dL^{-1} . The amount of sodium dithionite in the solution defines the oxygenation level, across a relevant range. e) Calibration curves corresponding to absorption at 1050 and 1200 nm measured in vitro. f) In vivo measurements of blood oxygen saturation as a function of time during changes in the concentration of oxygen (labeled in blue) in the surrounding environment. Results measured by the transient biosensor and commercial oximeter are labeled in black and green, respectively. g) Computed X-ray tomography (CT) image (processed by volume rendering analysis) of the transient biosensor implanted into a mouse at various stages of implantation from day 1 to day 15. The red arrow highlights the location of the transient biosensor, which is no longer visible under CT on Day 15. All the CT images share the same scale bar.

dissolution of the functional components (Si core and PLGA cladding). Promising approaches involve conformal encapsulation strategies based on bioresorbable materials such as silicon dioxide or silicon nitride. Further miniaturizing the device dimensions requires development of high-resolution techniques for patterning the PLGA cladding layer. Deploying advanced versions of these devices in animal model studies for both sensing (such as glucose concentration and oxygenation level) and stimulating, and extending the core concepts to other

classes of materials to enhance the range of passive and active photonic functionality represent two directions for future work.

Experimental Section

Optical and Spectroscopic Characterization: The optical testing used an assembly of optomechanical hardware (Ficontec, Inc., Figure S3a, Supporting Information), to align the fiber with the waveguide automatically using pattern recognition algorithms

(Figure S3b, Supporting Information). A tunable laser source (Keysight, Inc.) was used for the 1550 nm spectral band measurement. Another supercontinuum source (Super K, NKT Photonics Inc.) was used for the spectral band of 1100–1400 nm. The output was collected with a Newport power meter through a coupled fiber. Innovative grade US origin CD-1 mouse whole blood was purchased from Fisher Scientific, Inc. 2-Deoxy-D-glucose (99%, ACROS organics), ethanol, and deionized water were purchased from Sigma-Aldrich. A negative tone photoresist (SU8) was purchased from MicroChem. Measurements of the spectra of mouse blood with a range of glucose concentrations used a PDMS reservoir covered on top of a spiral waveguide biosensor, to confine 4 mL of mouse blood (intrinsic blood glucose concentration around 100 mg dL⁻¹) next to the sensor. A sheet of Parafilm sealed the top of the reservoir to prevent evaporation. Adding a controlled amount of aqueous glucose solution (80 μL of 1000 mg dL⁻¹) repeatedly to the reservoir using a micropipette yielded a range of glucose concentrations. A temperature controller maintained the system temperature at 24.0 ± 0.1 °C. For each case, spectral measurements were performed three times, ≈2 min after the addition of glucose solution.

Measurements of Blood Oxygen Saturation in Live Animal Models: All procedures associated with animal studies followed recommendations in the Guide for the Care and Use of Laboratory Animals of the National Institutes of Health. The Institutional Animal Care and Use Committee (IACUC) at Northwestern University (protocol IS00005877) approved the protocol. Female mice (CD1, age at initiation of the treatment: at least 6 weeks, but not more than 15 weeks, purchased from Charles River Laboratories) were acclimated up to 5 d before surgery. Animals were anesthetized using isoflurane gas during the implantation surgery and measurement. Following surgical exposure (Figure S16a, Supporting Information), a transient biosensor was inserted into the subcutaneous region near the thoracic spine (Figure S16b, Supporting Information). Bioabsorbable suturing and gluing closed the surgically exposed region with two bioresorbable fibers (labeled Fiber 1 and Fiber 2 in Figure 6a,c) probing externally. Each of the two fibers connected, via a fiber circulator, with a light source (1050 nm wavelength for Fiber 1, and 1200 nm wavelength for Fiber 2) and a power meter for delivering and detecting light, respectively. Comparing the absorption at 1050 and 1200 nm wavelength based on the Beer–Lambert law yielded the blood oxygen saturation.^[43] A commercial oximeter (PhysioSuite for Mice & Rats, Kent Scientific) placed at the hind paw of the mice monitors the blood oxygenation during the test. Staining with tungsten oxide nanopowders enabled the transient devices to be resolved under X-ray computed tomography.

Supporting Information

Supporting Information is available from the Wiley Online Library or from the author.

Acknowledgements

W.B. and H.Y. contributed equally to this work. W.Z. acknowledges support from Army Research Office under Grant No. W911NF-15-1-0035. Y.M. and X.F. acknowledge the support from the National Basic Research Program of China (Grant No. 2015CB351900) and the National Natural Science Foundation of China (Grant Nos. 11402135 and 11320101001). Y.H. acknowledges the support from National Science Foundation (Grant Nos. 1400169, 1534120, and 1635443) and National Institutes of Health (Grant No. R01EB019337). This work utilized Northwestern University Micro/Nano Fabrication Facility (NUFAB), which was partially supported by Soft and Hybrid Nanotechnology Experimental (SHyNE) Resource (NSF ECCS-1542205), the Materials Research Science and Engineering Center (NSF DMR-1121262), the State of Illinois, Northwestern University, and the Center for Bio-Integrated Electronics at the Simpson/Querrey Institute. The Center for Developmental Therapeutics was supported by Cancer Center Support

Grant P30 CA060553 from the National Cancer Institute awarded to the Robert H. Lurie Comprehensive Cancer Center.

Conflict of Interest

The authors declare no conflict of interest.

Keywords

flexible photonics, silicon nanomembrane, spectroscopy, transfer printing, transient photonics

Received: March 11, 2018

Revised: April 17, 2018

Published online: June 26, 2018

- [1] P. N. Prasad, *Introduction to Biophotonics*, John Wiley & Sons, Inc., Hoboken, NJ, USA **2004**.
- [2] V. R. Kondepati, H. M. Heise, J. Backhaus, *Anal. Bioanal. Chem.* **2008**, *390*, 125.
- [3] S. H. Yun, S. J. J. Kwok, *Nat. Biomed. Eng.* **2017**, *1*, 8.
- [4] S. L. Jacques, *Phys. Med. Biol.* **2013**, *58*, R37.
- [5] S. Nizamoglu, M. C. Gather, M. Humar, M. Choi, S. Kim, K. S. Kim, S. K. Hahn, G. Scarcelli, M. Randolph, R. W. Redmond, S. H. Yun, *Nat. Commun.* **2016**, *7*, 10374.
- [6] F. G. Omenetto, D. L. Kaplan, *Nat. Photonics* **2008**, *2*, 641.
- [7] R. Soref, *IEEE J. Sel. Top. Quantum Electron.* **2006**, *12*, 1678.
- [8] J. A. Rogers, T. Someya, Y. Huang, *Science* **2010**, *327*, 1603.
- [9] D.-Y. Khang, H. Jiang, Y. Huang, J. A. Rogers, *Science* **2006**, *311*, 208.
- [10] S.-W. Hwang, C. H. Lee, H. Cheng, J.-W. Jeong, S.-K. Kang, J.-H. Kim, J. Shin, J. Yang, Z. Liu, G. A. Ameer, Y. Huang, J. A. Rogers, *Nano Lett.* **2015**, *15*, 2801.
- [11] Y. Chen, H. Li, M. Li, *Sci. Rep.* **2012**, *2*, 622.
- [12] A. Ghaffari, A. Hosseini, X. Xu, D. Kwong, H. Subbaraman, R. T. Chen, *Opt. Express* **2010**, *18*, 20086.
- [13] Z. Qiang, H. Yang, L. Chen, H. Pang, Z. Ma, W. Zhou, *Appl. Phys. Lett.* **2008**, *93*, 61106.
- [14] X. Xu, H. Subbaraman, S. Chakravarty, A. Hosseini, J. Covey, Y. Yu, D. Kwong, Y. Zhang, W.-C. Lai, Y. Zou, N. Lu, R. T. Chen, *ACS Nano* **2014**, *8*, 12265.
- [15] W. Zhou, Z. Ma, H. Yang, Z. Qiang, G. Qin, H. Pang, L. Chen, W. Yang, S. Chuwongin, D. Zhao, *J. Phys. D: Appl. Phys.* **2009**, *42*, 234007.
- [16] D. Kwong, J. Covey, A. Hosseini, Y. Zhang, X. Xu, R. T. Chen, *Opt. Express* **2012**, *20*, 21722.
- [17] A. Shokrollahi, M. Zare, *Optik* **2013**, *124*, 855.
- [18] K. J. Yu, D. Kuzum, S.-W. Hwang, B. H. Kim, H. Juul, N. H. Kim, S. M. Won, K. Chiang, M. Trumpis, A. G. Richardson, H. Cheng, H. Fang, M. Thompson, H. Bink, D. Talos, K. J. Seo, H. N. Lee, S.-K. Kang, J.-H. Kim, J. Y. Lee, Y. Huang, F. E. Jensen, M. A. Dichter, T. H. Lucas, J. Viventi, B. Litt, J. A. Rogers, *Nat. Mater.* **2016**, *15*, 782.
- [19] S.-W. Hwang, H. Tao, D.-H. Kim, H. Cheng, J.-K. Song, E. Rill, M. A. Brenckle, B. Panilaitis, S. M. Won, Y.-S. Kim, Y. M. Song, K. J. Yu, A. Ameen, R. Li, Y. Su, M. Yang, D. L. Kaplan, M. R. Zakin, M. J. Slepian, Y. Huang, F. G. Omenetto, J. A. Rogers, *Science* **2012**, *337*, 1640.
- [20] L. Yin, A. B. Farimani, K. Min, N. Vishal, J. Lam, Y. K. Lee, N. R. Aluru, J. A. Rogers, *Adv. Mater.* **2015**, *27*, 1857.
- [21] L. M. Jurkić, I. Cepanec, S. K. Pavelić, K. Pavelić, *Nutr. Metab.* **2013**, *10*, 2.

- [22] S. Kang, R. K. J. Murphy, S. Hwang, S. H. S. M. Lee, D. V. Harburg, N. A. Krueger, J. Shin, P. Gamble, H. Cheng, S. Yu, Z. Liu, J. G. McCall, M. Stephen, H. Ying, J. Kim, G. Park, R. C. Webb, C. H. Lee, S. Chung, D. S. Wie, A. D. Gujar, B. Vemulapalli, A. H. Kim, K.-M. Lee, J. Cheng, Y. Huang, S. H. S. M. Lee, P. V. Braun, W. Z. Ray, J. A. Rogers, *Nature* **2016**, 530, 71.
- [23] F. Ramazani, W. Chen, C. F. Van Nostrum, G. Storm, F. Kiessling, T. Lammers, W. E. Hennink, R. J. Kok, *Int. J. Pharm.* **2016**, 499, 358.
- [24] H. K. Makadia, S. J. Siegel, *Polymers* **2011**, 3, 1377.
- [25] O. A. Shemesh, D. Tanese, V. Zampini, C. Linghu, K. Piatkevich, E. Ronzitti, E. Papagiakoumou, E. S. Boyden, V. Emiliani, *Nat. Neurosci.* **2017**, 20, 1796.
- [26] A. Leung, P. M. Shankar, R. Mutharasan, *Sens. Actuators, B* **2007**, 125, 688.
- [27] R. A. Potyrailo, S. E. Hobbs, G. M. Hieftje, *Fresenius' J. Anal. Chem.* **1998**, 362, 349.
- [28] B. D. Gupta, H. Dodeja, A. K. Tomar, *Opt. Quantum Electron.* **1996**, 28, 1629.
- [29] J. Workman, L. Weyer, *Practical Guide to Interpretive Near-Infrared Spectroscopy*, CRC Press, Boca Raton, FL **2008**.
- [30] S. F. Malin, T. L. Ruchti, T. B. Blank, S. N. Thennadil, S. L. Monfre, *Clin. Chem.* **1999**, 45, 1651.
- [31] SIMULIA, ABAQUS Analysis User's Manual, **2010**.
- [32] P. Gentile, V. Chiono, I. Carmagnola, P. V. Hatton, *Int. J. Mol. Sci.* **2014**, 15, 3640.
- [33] R. G. Hunsperger, *Integrated Optics*, Springer, New York **2009**, pp. 107–128.
- [34] R. Ramponi, R. Osellame, M. Marangoni, *Rev. Sci. Instrum.* **2002**, 73, 1117.
- [35] Y. A. Vlasov, S. J. McNab, *Opt. Express* **2004**, 12, 1622.
- [36] K. K. Lee, D. R. Lim, L. C. Kimerling, J. Shin, F. Cerrina, *Opt. Lett.* **2001**, 26, 1888.
- [37] D. A. Woods, C. D. Bain, *Soft Matter* **2014**, 10, 1071.
- [38] L. Tombez, E. J. Zhang, J. S. Orcutt, S. Kamlapurkar, W. M. J. Green, *Optica* **2017**, 4, 1322.
- [39] X.-B. Wang, M.-H. Jiang, S.-Q. Sun, J.-W. Sun, Y.-J. Yi, C.-M. Chen, X.-Q. Sun, F. Wang, Z.-C. Cui, D.-M. Zhang, *RSC Adv.* **2016**, 6, 50166.
- [40] G. M. Reaven, *Diabetes* **1988**, 37, 1595.
- [41] H.-C. Wang, A.-R. Lee, *J. Food Drug Anal.* **2015**, 23, 191.
- [42] J. Yadav, A. Rani, V. Singh, B. M. Murari, *Biomed. Signal Process. Control* **2015**, 18, 214.
- [43] R. N. Pittman, *Regulation of Tissue Oxygenation*, Morgan & Claypool Life Sciences, Williston, VT, USA **2011**.